Properties of Nanocrystalline Nickel Particles in Ni-SiO_2 Composites

G. Ennas, A. Falqui[a], G. Piccaluga, S. Solinas, D. Gatteschi[b], C. Sangregorio[b], and A. Benedetti[c]

Dipartimento di Scienze Chimiche, Università di Cagliari, 09100 Cagliari, Italy
[a] Dipartimento di Fisica, Università di Cagliari, Italy
[b] Dipartimento di Chimica, Università di Firenze, Italy
[c] Dipartimento di Chimica Fisica, Università di Venezia, Italy

Reprint requests to Prof. G. E; Fax: +39 070 6754388, E-mail: ennas@unica.it

Z. Naturforsch. **55 a,** 581–588 (2000); received March 9, 2000

Nickel-Silica nanocomposites with a nickel content equal to 10, 15, 20 wt% have been prepared by a sol-gel method starting from ethanolic solutions of tetraethoxysilane and nickel nitrate hexahydrate. After gelation the samples were reduced in H_2 flow at selected temperature (450 °C < T < 600 °C).

The morphological, structural and magnetic properties were investigated by transmission electron microscopy (TEM), wide and small angle X-ray scattering (WAXS, SAXS), magnetic susceptibility in zero field cooled and field cooled mode (ZFC and FC), and magnetic hysteresis loop.

Nanometric nickel particles are observed in all the investigated samples. TEM, WAXS and SAXS techniques indicate that the average nickel particle size grows slightly but almost regularly with the nickel concentration. TEM results moreover indicate that also the width of the particle size distribution, which can be simulated by log-normal functions, follows this trend.

All the sample treated in hydrogen show superparamagnetic behaviour. The magnetisation falls to reach saturation up to highest measuring field of 70 kOe even at 3 K, while the observed coercivity H_c is much higher than the theoretical bulk one. Some uncertainty in the complete interpretation of the sequence of magnetic measurements is attributed to a progressive oxidation of the samples when these are air exposed.

Key words: Nanocomposites; Nickel-Silica; X-ray Diffraction; TEM; Magnetic Properties.

1. Introduction

In nanotechnology, the dispersion of nanoparticles in inert matrices has been widely adopted either to stabilise the nanoparticles or to modify their physicochemical properties [1 - 4]. Recently our interest has been devoted to Ni-SiO_2 nanocomposites, that are attractive because of their magnetic, electrical and optical properties [5 - 8]. Since the behaviour of these materials is strongly dependent on the composition, the sizes of the constituent particles and their size distribution, several methods have been developed to prepare, control and vary such characteristics in order to meet the needs of the end user [9 - 24]. Sol-gel methods in particular have shown to be effective in producing nanocrystalline phases dispersed in amorphous silica. Moreover, sol-gel processes have the advantage that their extension to large-scale and high-rate production is relatively simple.

In a recent paper the sol-gel preparation of nanometric nickel particles homogeneously dispersed over silica support has been described [25]. The main parameters affecting the preparation have been investigated and a way to prepare very small particles even in composites with high nickel content has been found.

The present paper reports the study of three nanocomposites Ni-SiO_2 with different nickel content. The explored range of composition was 10-20wt%, where previous studies indicated good results of the preparation procedure. The goals of the work were a careful determination of the morphological and structural characteristics of the samples (shape, size, size distribution, nature of the formed particles) and an investigation of the magnetic properties of the nanocomposites that in turn depend on the mentioned characteristics. For the former purpose wide and small angle X-ray scattering (WAXS and SAXS) experiments and transmission electron microscopy (TEM)

0932–0784 / 00 / 0600–0581 $ 06.00

observations were performed, while the magnetic behaviour was characterised by the measurement of magnetic susceptibilities, magnetisation values and hysteresis loops.

2. Experimental

2.1. Sample Preparation

The samples were prepared by the sol-gel technique, using ethanol (EtOH, C. Erba 95%), nickel nitrate hexahydrate (Aldrich 98%) and tetraethyl orthosilicate (TEOS, Aldrich 98%). The molar ratios of EtOH/TEOS was 10:1. The nickel salt was added to the mixture in order to obtain Ni-SiO_2 samples with 10, 15, 20 metal weight%. The hydrolysis reaction was promoted by the water present in the salt and in EtOH 95%. In a typical preparation the sol was obtained by rapidly mixing an acid ethanolic solution of the nickel salt and an ethanolic TEOS solution. The pH of the starting sol mixture was kept in the range 0-1 by adding few drops of 70% nitric acid (C. Erba). The solution was stirred at 18-20 °C for 1 hour. The obtained clear sol was then poured into a Teflon beaker and allowed to gel in air at room temperature (RT). Powdered dry gel was put under flowing hydrogen, heated to a chosen temperature (450 ° - 650 °C) and kept there for the preset reduction time. Then the furnace was allowed to cool down to room temperature (RT). In order to manipulate the reduced pyrophoric powders in air, at the end of the reduction treatment at RT the hydrogen was replaced by a slow commercial argon flow (impure by some ppm of oxygen). This operation passivates the superficial layer of the particles and protects the bulk metal particles from rapid combustion.

In the following, the samples will be indicated as Ni_xY^z where Y stands for the treatment temperature (T_{treat}), z for the time of treatment in minutes and x for the nickel concentration in weight percent.

2.2. WAXS Measurements

The data were collected at RT with a Siemens D500 $\vartheta/2\vartheta$ powder diffractometer using MoKα radiation, a graphite monochromator on the diffracted beam and a scintillation counter with pulse-height discriminator. XRD patterns were recorded in step scan mode in the range $4° \leq 2\theta \leq 45°$ with step size 0.04°. Ni 111 and Ni 222 peaks were scanned with step size 0.02° from 2ϑ = 16 to 26° and from 36 to 44°, respectively, collecting at least 5,000 counts for each step. The divergence and receiving slits were chosen in order to ensure a high resolution mode for the crystalline phases. The instrumental profile parameters were derived from the fitting of powder XRD data obtained from a standard sample. The crystalline peak profiles were represented by pseudo-Voigt functions, and the correction function for asymmetry was applied. X-ray line profile analysis was performed according to the Warren-Averbach (W-A) method for size and strain determination [26]. A rough estimation of the crystallite size distribution from the second derivative of Fourier coefficients was also obtained.

2.3. SAXS Measurements

The small angle X-ray scattering data were obtained with a Kratky camera in the "quasi-infinite slit" geometry, equipped with an electronic step scanner. A pulse height discriminator and proportional counter were also employed. Ni-filtered CuKα radiation was used. The intensities were measured by determining the time necessary to accumulate 2×10^4 counts for each scattering angle. The corrected intensities were obtained by subtracting the instrumental background corrected for sample absorption. They are given in terms of the momentum transfer $h = (4\pi/\lambda)\sin(\theta/2)$ (with λ = wavelength and θ the scattering angle).

The silica scattering (obtained under the same condition as the nickel doped samples) was subtracted from the total scattering curves of the three samples after their normalisation on the same scale [27].

2.4. TEM Measurements

TEM observation were carried out directly on the as-prepared powders without any thinning procedure using a JEOL 200CX microscope operating at 200 kV; powders were ultrasonically dispersed in octane (C. Erba 99%) and deposited on a carbon grid.

2.5. Magnetic Measurements

Static magnetic susceptibilities were measured with a Metronique Ingeniérie MS02 SQUID magnetometer, equipped with a superconducting magnet capable of producing fields up to 8 T. Zero-field-cooled (ZFC) magnetisations were measured by cooling the

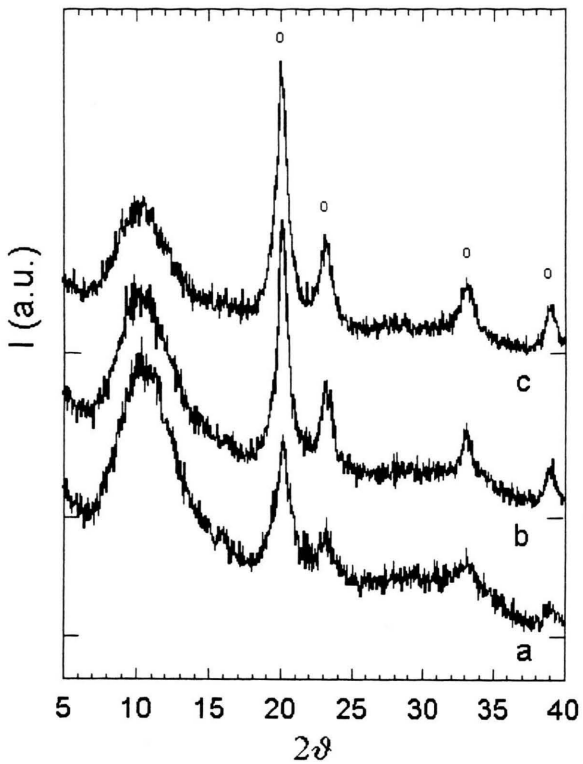

Fig. 1. WAXS spectra of Ni_x650^{240} samples: a) x = 10, b) x = 15, c) x = 20. (o) Ni.

sample in zero field and then by increasing the temperature with an applied field of 50 Oe, while field cooled curves (FC) were collected by cooling the sample in the measuring field of 50 Oe.

3. Results and Discussion

3.1. WAXS

WAXS spectra of the Ni_x650^{240} samples for x = 10, 15, 20 wt% are reported in Figure 1. Broad peaks of crystalline nickel fcc phase [28] are present over the diffuse haloes of amorphous silica. As expected, the peak height increases with nickel content; moreover, a light sharpening of the metal peaks along the series is observed, which indicates an increase in the average size of the particles. The average particle sizes ($\langle D_{waxs} \rangle$), obtained by the Warren-Averbach analysis, carried out on the 111/222 pairs and reported in Table 1, confirm this trend. No significant strain or stress ($\langle e^2 \rangle^{1/2}$ less than 10^{-4}) values were calculated by Warren-Averbach methods in 15 and 20 wt% samples (in 10 wt% the separation strain/size was not made because of the too small 222 peak signal). The full width at half maximum (FWHM) obtained by the calculated rough size distributions is around 4 nm for all samples.

Table 1. Average particle size ($\langle D_{TEM} \rangle$) and standard deviation (σ_{TEM}) of log-normal distribution obtained by TEM, average particle size ($\langle D_{SAXS} \rangle$) obtained by SAXS, average particle size ($\langle D_{WAXS} \rangle$) obtained by WAXS. Average particles size in nm. The estimated deviation of the parameters is given in parentheses as uncertainty on the last digit.

Sample	$\langle D_{TEM} \rangle$	σ_{TEM}	$\langle D_{SAXS} \rangle$	$\langle D_{WAXS} \rangle$
$Ni_{10,650}$	5.6(2)	0.27(2)	6.2(6)	2.0(2)
$Ni_{15,650}$	6.4(2)	0.26(2)	7.5(7)	3.6(4)
$Ni_{20,650}$	7.1(2)	0.33(2)	8.4(8)	3.9(4)

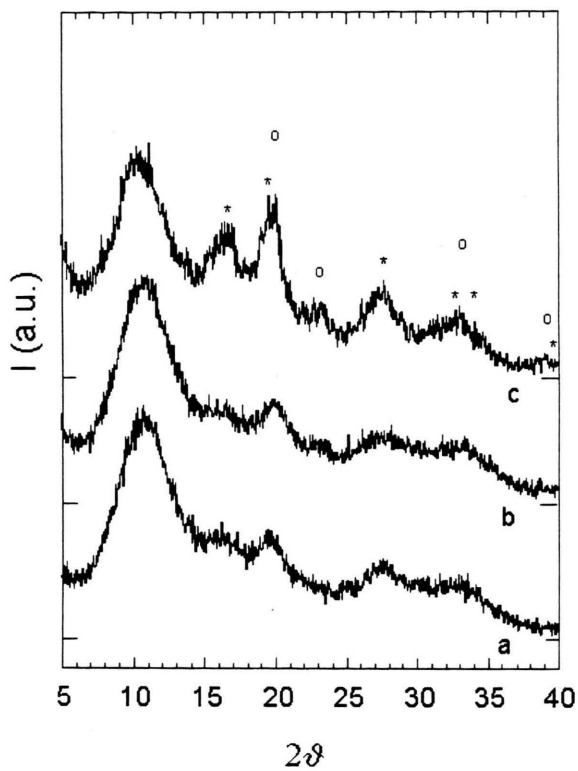

Fig. 2. WAXS spectra of Ni_x450^{30} samples: a) x = 10, b) x = 15, c) x = 20. (*) NiO, (o) Ni.

No appreciable NiO peaks [29] are visible in the spectra of Fig. 1, indicating that in freshly reduced Ni_x650^{240} samples either the oxidation concerns the superficial layer only, or only very small oxide particles are formed. WAXS spectra of Ni_x450^{30} for x = 10, 15, 20 wt% are reported in Figure 2. These patterns

show that, using these mild thermal conditions, the reduction process is rather incomplete and only faint broad nickel fcc peaks are present; in all Ni_x450^{30} samples, broad peaks due to nickel oxide are still evident together with the amorphous silica haloes. The nickel oxide particle sizes obtained by Warren-Averbach analysis give 1.2, 2.4, 3.3 nm for Ni_x450^{30} with x = 10, 15, 20 wt% respectively. Finally, neither nickel silicate nor nickel silicide were observed in our samples.

3.2. SAXS

In Fig. 3 the Porod plots of the three Ni_x650^{240} SAXS intensities are reported. The subtraction of the scattering due to the silica from the total intensities of the nanocomposites does not give any interference effect, so the resulting intensities can be used to study the microstructural features of the metallic phase. The shifts of the maximum of the SAXS curves towards lower h values indicate a little growth of the particles. The average particle size D can be roughly estimated directly from Fig. 3 through the simple relation $D = 2\pi/h_{max}$, were h_{max} denotes the h value of the maximum [30]. A more careful determination of the volume weighted average size was obtained by fitting the calculated scattering intensities to the experimental data using a Schultz distribution of spheres [31]. The small angle intensity scattered by a dilute system of a continuous normalised distribution $P(r)$ of particles with radius r can be represented by the monotonically decreasing curve given by

$$I(h) = \frac{N_p}{V}\Delta\rho^2 \int P(r)\sigma^2(h,r)\,\mathrm{d}\,r,$$

where N_p is the number of particles, V the irradiated sample volume, $\Delta\rho$ the electronic density difference between particle and matrix, and $\sigma^2(h,r) = V^2(r)S^2(h,r)$ the differential scattering cross section of a single particle, $V(r)$ is the particle volume and $S^2(h,r)$ the particle form factor. In the case of spherical particles

$$S(h,r) = 3\frac{\sin(hr) - hr\cos(hr)}{(hr)^3}$$

$P(r)$ is a normalized Schultz distribution

$$P(r) = \frac{1}{\Gamma(z+1)}\left(\frac{z+1}{\langle r\rangle}\right)^{z+1} r^z \exp\left(-\frac{z+1}{\langle r\rangle}\right),$$

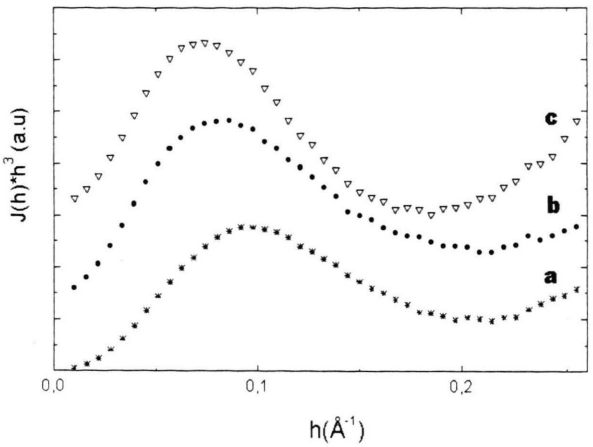

Fig. 3. SAXS Porod plot of Ni_x650^{240} samples: a) x = 10, b) x = 15, c) x = 20.

where z (with $z > -1$) is the form parameter of the distribution.

The Schultz function has been chosen because of its ability to describe different distribution shapes, while the spherical shape has been used on the ground of TEM observations. Yet, these particular choices do not affect the main features of the final results [32].

The average particle sizes ($\langle D_{SAXS}\rangle$), reported in Table 1, were respectively 6.2 nm for sample $Ni_{10}650^{240}$, 7.5 nm for sample $Ni_{15}650^{240}$, and 8.4 nm for sample $Ni_{20}650^{240}$. The error for each size is in the range of 10 - 15%.

3.3. TEM

The occurrence of almost spherical nickel metallic particles is observed in TEM micrographs. The particles do not cluster and are uniformly dispersed in the amorphous silica matrix. In order to obtain an accurate estimation of the average particles size, $\langle D_{TEM}\rangle$, at least 300 particles for each sample were counted in the micrographs. Several authors [33 - 35] have suggested that the obtained histograms of size, in a nanoparticles assembly, can be fitted by a log-normal distribution function

$$P(D) = 1/(\sqrt{2\pi}D\sigma)\exp[-1/(2\sigma^2)(\ln D/D_0)^2],$$

where σ is the standard deviation and D_0 the mean diameter (the median), while the average particle size $\langle D_{TEM}\rangle$ is defined by

$$\langle D_{TEM}\rangle = D_0\exp(\sigma^2/2).$$

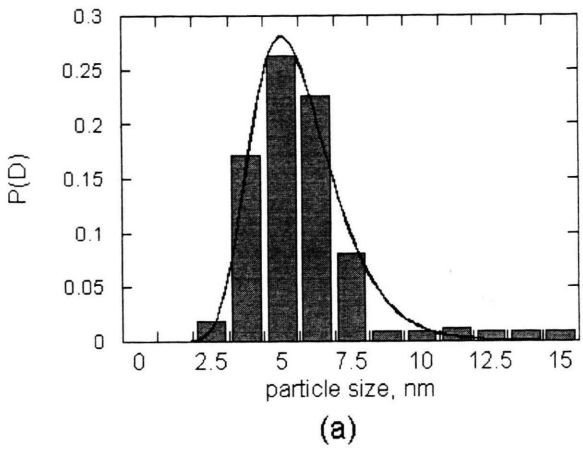

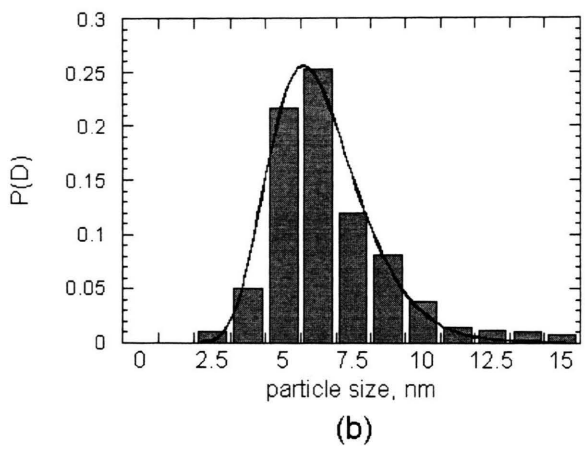

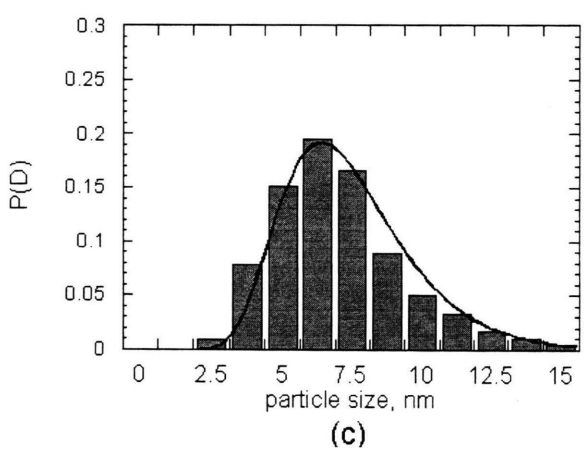

Fig. 4. TEM hystograms and log-normal fit for Ni_x650^{240} samples: a) $x = 10$, b) $x = 15$, c) $x = 20$.

The histogram and corresponding fitting curves for the Ni_x650^{240} samples are shown in Fig. 4, while

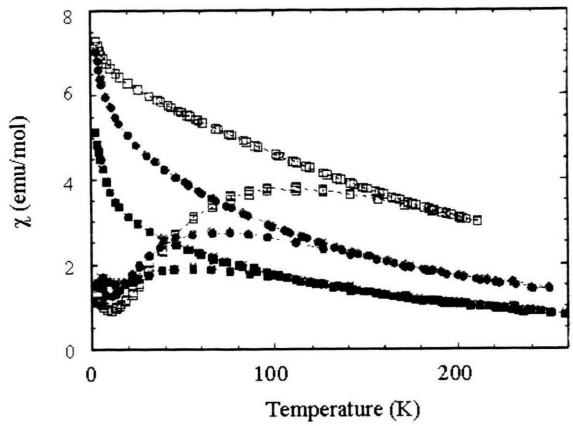

Fig. 5. Temperature dependence of the ZFC and FC magnetic susceptibilites of Ni_x650^{240} samples: $x = 10$ (■), $x = 15$ (□), $x = 20$ (●). The measurements were performed with an applied field of 50 Oe.

$\langle D_{TEM} \rangle$ and σ values are reported in Table 1. The results from TEM examination and SAXS measurements are in good agreement. However, TEM reveals that in the $Ni_{20}650^{240}$ sample the standard deviation is larger than in the other two samples, indicating a broader size distribution.

3.4. Magnetic Measurements

In Fig. 5 the ZFC and FC curves for samples of the Ni_x650^{240} series are shown. In all the samples, the ZFC and FC susceptibilities coincide at high temperature, while at lower temperatures they start to separate: the FC magnetisation increases on decreasing the temperature, while the ZFC magnetisation shows a broad maximum. Such behaviour is characteristic of superparamagnetism [36 - 37], i. e. of the temperature-dependent blocking of the magnetisation of particles whose size determines a magnetic anisotropy comparable to thermal energy. Since the anisotropy is in a first approximation proportional to the volume of the particles, the blocking-deblocking process is different for particles of different size. The maximum temperature in the ZFC curve (T_{max}) is related in a complex way to the blocking of particles with average volume, while the temperature at which the ZFC and FC curves start to separate (T_{sep}) corresponds to the blocking of the largest particles. The observed behaviour is a clear confirmation of the nanometer size of the particles [38].

Fig. 5 shows that no correlation is observed between the nickel concentration and the size of

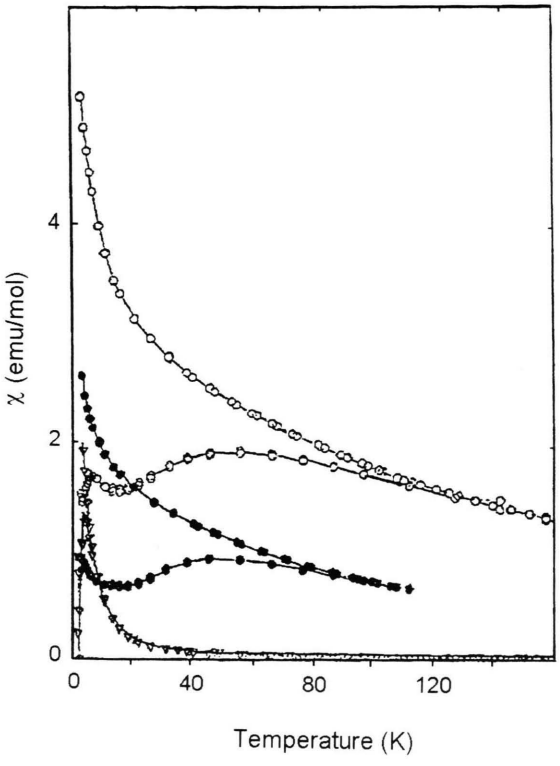

Fig. 6. Temperature dependence of the ZFC and FC magnetic susceptibilites of samples $Ni_{10}Y^{30}$ with Y = 450 (Δ), 550 (•), 650 (o). The measurements were performed with an applied field of 50 Oe.

nanoparticles. In fact $Ni_{15}650^{240}$ displays higher values both of T_{max} and T_{sep}, thus suggesting that this sample contains larger particles with a broader distribution than both the $Ni_{10}650^{240}$ and $Ni_{20}650^{240}$ samples. However in all the samples the ZFC curve is broad, while T_{max} and T_{sep} are well separated from one another. This behaviour is a clear indication that our nanophase systems have a broad size distribution.

A similar behaviour was observed for samples treated at lower temperature with some important difference: i) the ZFC susceptibility of $Ni_{10}450^{30}$ samples (Fig. 6) displays a sharp peak at low temperature (below 10 K), ii) on increasing T_{treat}, a second peaks appears in the ZFC curve; both the maximum in the ZFC curve (T_{max}) and the temperature where thermal magnetic irreversibility appears (T_{sep}) increase with T_{treat}, iii) for each series with the same nickel content the χT product increases when T_{treat} is increased. These observations confirm that, in order to prepare metallic nickel nanoparticles, reduction temperatures higher than 450 °C are required. In fact

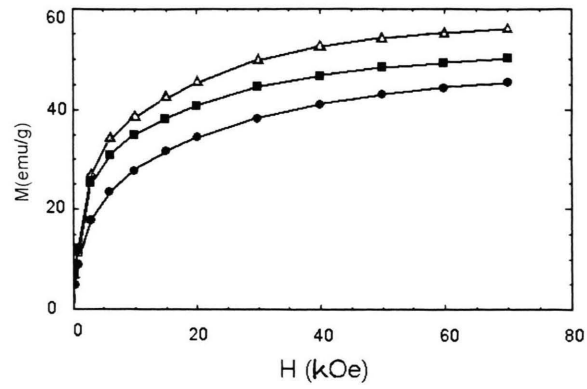

Fig. 7. Magnetisation versus applied magnetic fields curves of Ni_x650^{240} samples: x = 10 (•), x = 15 (■), x = 20 (Δ). The isothermal magnetisation were collected at T = 3K.

the magnetic behaviour of Ni_x450^{30} samples suggests that they essentially consist of very small antiferromagnetic nickel oxide nanoparticles ($D \approx 1 \div 3$ nm) dispersed in the silica matrix. We remind that antiferromagnetic ultrafine particles possess a non-zero magnetisation that originates from uncompensated surface spins [39] or from a finite size effect [40]. This net magnetic moment should give rise to a weak ferromagnetism and to a superparamagnetic behaviour, as observed in our case.

On increasing T_{treat} above 450 °C, a large increase of the blocking temperature and of the χT product is observed, indicating the appearance of metal nanoparticles. The trend of T_{max} and T_{sep} indicates that the sizes of the particles increase with T_{treat} up to 650 °C, while the distribution becomes broader. The persistence of a low T peak in the ZFC curve, as well as the non saturation of the low temperature FC magnetic susceptibility, suggest that very small particles, presumably of NiO, still occur also in the Ni_x650^{240} samples.

Figure 7 shows the isothermal magnetisation curves measured for the Ni_x650^{240} samples at 3K. The magnetisation falls to reach saturation up to the highest measuring field of 70 kOe even at 3 K. This can be due either to the presence of very small particles that are still relaxing even at this low temperature, or to the non-collinear spin structure of the disordered surface layer [41], or to the occurrence of some antiferromagnetic NiO.

Hysteresis loops were measured in the range +70 kOe –70 kOe. At 3 K a hysteretic behaviour is observed for all the samples of the Ni_x650^{240} series. The

Table 2. Maximum temperature (T_{max}) in the ZFC curves and temperatures at which the FC and ZFC curves start to separate (T_{sep}), Saturation Magnetisation (M_s), Residual Magnetisation/Saturation Magnetisation (M_r/M_s) and Coercivity (H_c).

Sample	T_{max} (K)	T_{sep} (K)	M_s (emu/g)	M_r/M_s	H_c (Oe)
$Ni_{10,650}$	55	132	51.7	0.19	510
$Ni_{15,650}$	110	180	53.3	0.24	790
$Ni_{20,650}$	70	130	58.2	0.26	960

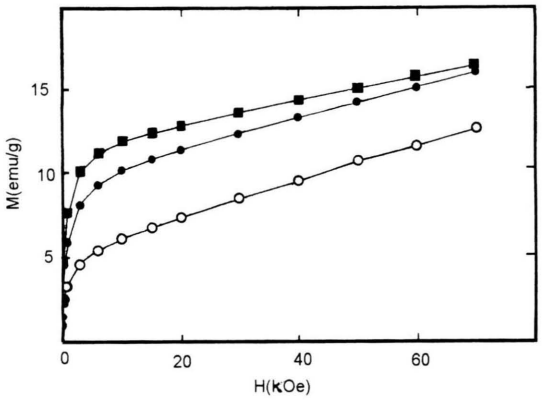

Fig. 8. Magnetisation versus applied magnetic fields curves of Ni_x650^{240} samples: $x = 10$ (o), $x = 15$ (■), $x = 20$ (●). The isothermal magnetisation were collected at $T = 125$ K.

values of coercive fields and the reduced remanences (M_r/M_s) are reported in Table 2.

The reduced remanence increases with the metal content, but its values are always lower than those expected for a system of randomly oriented, non-interacting, single domain particles in the blocked state. This result confirms that at this temperature there is a large fraction of fast relaxing superparamagnetic nanoparticles. On increasing the metal concentration also the coercivity strongly increases: it is 510 Oe for $Ni_{10}650^{240}$ while it is near to 1000 Oe for $Ni_{20}650^{240}$. The measured coercivities are much higher than the value of the bulk, as it should be expected for single domain particles, where the reversal of the magnetisation occurs through a coherent rotation of all the spins.

Finally we point out that the measured coercivities indicate that progressively larger particles are present when the metal concentration is increased. The same indication is given by the higher values of M_s evaluated from the magnetisation curves. This observation is contrary to the trend of T_{max} observed in the ZFC experiments. A possible interpretation of this discrepancy can be proposed by taking into account that at 125 K the magnetization curves for Ni_x650^{240} (Fig. 8) have the same "non regular" trend as the ZFC-FC curves. This crossover of magnetisation curves could derive from a different form of the size distribution function P(D) in the samples. However this hypothesis seems in contrast with the experimental distribution curve obtained by TEM. Then a second factor could be a different oxidation level of the samples. Magnetic measurements were performed at different times while the samples were air exposed. Therefore the oxidation process may have affected the effective size distribution of the metal core of the nanoparticles, which is the one that mainly determines the magnetic properties of the assembly [16].

4. Conclusions

All the methods used indicate that the experimental procedure provides nanometric nickel particles; their average sizes vary slightly but regularly with the concentration. The particle size by SAXS and TEM measurements is greater than that by WAXS determination, as expected. In fact, WAXS determines the extent of coherently diffracting domains, while SAXS and TEM determine the extent of isoelectronic density domains, which are generally greater than the previous ones. Normally, the difference between the evaluations of an average particle size by WAXS and by SAXS and TEM is less marked. Probably, in this case the smaller value of the average particle size calculated by WAXS is due to the presence of a layer of nickel oxide around the particles, that reduces the effective size of the nickel metal particles.

Magnetic measurements of the three samples treated at the highest temperature (650 °C), evidenced superparamagnetic behaviour, which points out that the particle size is in the nanometric range. However a detailed interpretation of the magnetic data can not be provided, the data analysis being hindered by the oxidation of the metal nanoparticles. Magnetic measurements were in fact performed at different times with respect to the other techniques, while the samples were air exposed. The silica matrix does not prevent the particle from oxidation to NiO. Furthermore, once the surface has been transformed to NiO, the oxide does not protect the particles from a complete oxidation, as it has been observed in other nanophase

systems based on metal nanoparticles [14, 16, 42]. Therefore the oxidation process may have strongly affected the effective size distribution of our metal-based nanocomposites.

Acknowledgements

This work has been supported by CNR, MURST and ENEA.

[1] J. Komarneni, J. Mater. Chem **2**, 1219 (1992).
[2] R. E. Newnham, S. E. McKinstry, and H. Ikawa, Mat. Proc. Soc. Symp. **175**, 161 (1990).
[3] E. Tronc, Il nuovo Cimento **18**, 163 (1996).
[4] S. Roy and D. Chakravorty, J. Mat. Res. **9**, 2314 (1994).
[5] J. P. Wang and H. L. Luo, J. Magn. Magn. Mater. **54**, 131 (1994).
[6] A. Corrias, G. Paschina, and P. Sirigu, J. Non-Cryst. Solids **232**, 358 (1998).
[7] S. De, M. Gusso, L. Topfer, M. Catalano, F. Gonella, G. Mattei, P. Mazzoldi, and G. Battaglin, J. Appl. Phys. **80**, 6734 (1996).
[8] S. Roy, D. Das, D. Chakravorty, and D. C. Agraval, J. Appl. Phys. **74**, 4746 (1993).
[9] K. Tohji, Y. Udagawa, S. Tanabe, and A. Ueno, J. Amer. Chem. Soc. **106**, 613 (1984).
[10] E. J. Shiu and M. Keane, J. Catal. **173**, 450 (1998).
[11] D. L. Leslie-Pelecky and R. D. Rieke, Chem. Mater. **8**, 1770 (1996).
[12] J. W. E. Coenen, Appl. Catal. **54**, 65 (1989).
[13] V. C. H. Kroll, H. M. Swaan, S. Lacombe, and C. Mirodatos, J. Catal. **164,** 387 (1997).
[14] C. Estournes, T. Lutz, J. Happich, T. Quaranta, P. Wissler, and J. L. Guille, J. Magn. Magn. Mater. **173**, 89 (1997).
[15] A. Corrias, G. Ennas, A. Musinu, G. Paschina, and D. Zedda, J. Mater. Res. **12**, 2767 (1997).
[16] S. Sako, K. Ohshima, M. Sakai, and S. Bendow, J. Vac. Sci. Tech. **B15**, 1338 (1998).
[17] J. J. Gamman, J. Chem. Soc. Farad. Trans **94**, 701 (1998).
[18] M. Falconieri G. Salvetti, E. Cararuzza, F. Gfonella, P. Mazzoldi, M. Piovesan, G. Battaglin, and R. Polloni, App. Phys. Lett. **73**, 288 (1998).
[19] C. Louis, Z. X. Cheng, and M. Che, J. Phys. Chem. **97**, 5703 (1993).
[20] O. Clause, M. Kermarec, L. Bonneviat, F. Villain, and M. Che, J. Amer. Chem. Soc. **114**, 4709 (1992).
[21] P. Burattin, M. Che, and C. Louise, J. Phys. Chem b**101** 7060 (1997).
[22] A. Basumallick, K. Biswas, G. C. Das, and S. Mukherjie, J. Mater. Res. **10**, 2938 (1995).
[23] G. Ennas, A. Musinu, G. Piccaluga, D. Zedda, D. Gatteschi, C. Sangregorio, J. L. Stanger, G. Concas, and G. Spano, Chem. Mater. **10**, 495 (1998).
[24] F. del Monte, M. P. Morales, D. Levy, A. Fernandez, M. Ocaña, A. Roig, E. Molins, K. O'Grady, and C. J. Serna, Langmuir **13**, 3627 (1997).
[25] G. Ennas, A. Mei, A. Musinu, G. Piccaluga, G. Pinna, and S. Solinas, J. Non-Cryst. Solids **232**, 587 (1998).
[26] B. E. Warren X-Ray Diffraction, Addison Wesley, Reading MA 1969, p. 264.
[27] P. Riello and A. Benedetti, J. Chem. Phys. **106**, 8660 (1997).
[28] JCPDF card n° 4-854, International Center for Diffraction Data, Swarthmore, PA (USA).
[29] JCPDF card n° 4-835 and 22-1189, International Center for Diffraction Data, Swarthmore, PA (USA).
[30] S. Ciccariello, A. Benedetti, F. Pinna, G. Strukul, W. Juszczyk, and H. Brumberger, Phys. Chem. Chem. Phys **1**, 367 (1999).
[31] A. Benedetti, J. Appl. Cryst. **37**, 647 (1997).
[32] H. Brumberger, J. Goodisman, R. Ramaya, and S. Ciccariello, J. Appl. Cryst. **29**, 526 (1996).
[33] R. W. Chantrell, J. Popplewell, and S. W. Charles, Physica **86-88B**, 1421 (1977).
[34] K. O'Gready and A. Bradbury, J. Magn. Magn. Mater. **38**, 91 (1994).
[35] N. Moumen and M. P. Pileni, Chem. Mater. **8**, 1128 (1996).
[36] A. H. Morrish The Physical Principle of Magnetism, J. Wiley & Sons, New York 1965.
[37] L. Néel, Ann. Geophys. **5**, 99 (1949).
[38] J. F. Loffler, J. P. Meier, B. Doudin, J. P. Ansermet, and W. Wagner, Phys. Rev. B **57**, 2915 (1998).
[39] L. Néel, Compt. Rend. (Paris). **252**, 4075 (1961).
[40] R. H. Kodama, S. A. Makhlouf, and A. E. Berkowitz, Phys. Rev. Lett. **79**, 1393 (1997).
[41] E. Tronc, P. Prene, J. Jolivet, F. d'Orazio, F. Lucari, D. Fiorani, M. Godinho, R. Nogues, and J. L. Dormann Hyperf. Interact. **95**, 129 (1995).
[42] S. Gangopadhyay, and G. C. Hadjipanayis, C. M. Sorensen, and K. J. Klabunde, J. Appl. Phys. **73**, 6964 (1993).